Astron. Astrophys. 349, 323–333 (1999)

ASTRONOMY AND ASTROPHYSICS

Diffusive shock acceleration in extragalactic jets

M. Micono[1], **N. Zurlo**[2], **S. Massaglia**[1], **A. Ferrari**[1], **and D.B. Melrose**[3]

[1] Dipartimento di Fisica Generale dell'Università, Via Pietro Giuria 1, I-10125 Torino, Italy
[2] Dipartimento di Ingegneria Aeronautica e Spaziale, Politecnico di Torino, Corso Duca degli Abruzzi 24, I-10129 Torino, Italy
[3] Research Centre for Theoretical Astrophysics, School of Physics, University of Sydney, NSW 2006, Australia

Received 17 December 1998 / Accepted 23 June 1999

Abstract. We calculate the temporal evolution of distributions of relativistic electrons subject to synchrotron and adiabatic processes and Fermi-like acceleration in shocks. The shocks result from Kelvin-Helmholtz instabilities in the jet. Shock formation and particle acceleration are treated in a self-consistent way by means of a numerical hydrocode. We show that in our model the number of relativistic particles is conserved during the evolution, with no need of further injections of supra-thermal particles after the initial one. From our calculations, we derive predictions for values and trends of quantities like the spectral index and the cutoff frequency that can be compared with observations.

Key words: acceleration of particles – hydrodynamics – instabilities – shock waves – galaxies: jets

1. Introduction

Observations of non-thermal astrophysical sources upon the utmost diverse spatial scales and luminosity ranges, from Supernova remnants to Active Galactic Nuclei, and energy bands, from radio frequencies up to $\gamma-$rays, require electron acceleration up to ultra-relativistic energies when interpreted via synchrotron or self-Compton emission. Relativistic particles can also be directly detected as in the case of the streams of particles from solar flares or the cosmic radiation.

Multi-wavelength studies of extragalactic jets, performed by combining observations from radio arrays, HST in the optical band and X-ray satellites, showed that many extragalactic jets emit non-thermal radiation extending from radio to X-rays, and that spectral and morphological features remain, in many instances, nearly constant along the jet from radio up to optical frequencies. This implies a constancy of the relativistic electron distribution function over at least five decades in energy, that needs to be interpreted (see discussions in Meisenheimer et al. 1996 and Meisenheimer et al. 1996 for M87).

Many physical mechanisms of particle acceleration have been studied, and Fermi-like processes occurring at MHD shocks have been particularly visited since they automatically lead to power-law particle distributions, as dictated by observations (see, e.g., Bell 1978, Drury 1983, Blandford & Eichler 1987, Achterberg 1990, Kirk 1994). Other mechanisms of particle acceleration include the diffusive particle acceleration at a tangential discontinuity in a velocity field involving relativistic velocities (Ostrowski, 1990, 1998). Continuous reacceleration of particles could take place by conversion of magnetic energy into particle energy via magnetic reconnection, as proposed by Lesch & Birk (1998); mechanisms of particle acceleration by turbulent plasma waves (Li et al. 1997) or by intense long-wavelength electromagnetic fields (Bisnovatyi-Kogan & Lovelace 1995) have also been considered. Each of these mechanisms leads to different values for the maximum energy attained by the accelerated particles, and different predictions on the observed radiation spectrum.

A possible clue to build a "universal spectrum" is the diffusive shock acceleration (DSA) by multiple shocks, as discussed in Melrose & Pope (1993) and Ferrari & Melrose (1997), under very general conditions.

In this paper we concentrate on the diffusive particle acceleration at shocks, and we treat, in a consistent way by means of a numerical hydrocode, the jet instabilities that yield shock formation, the particle acceleration in these shocks, and the temporal evolution of the distribution function, subject to adiabatic effects and synchrotron losses. In our model the magnetic field and the relativistic particles are advected passively by the thermal fluid, as in previous studies by Matthews & Scheuer (1990a and 1990b) who treated adiabatic expansion and synchrotron losses without including particle acceleration, and by Massaglia et al. (1996) who modeled shock acceleration as an adiabatic compression of fixed strength. In our study the equation for the evolution of the particle energy spectrum is solved in a self-consistent way, and particle acceleration at shocks is treated in the 'test-particle' approximation, i.e. neglecting the effects of energy subtraction from the shocks. Moreover we concentrate on the stability and radiative properties of the jet beam, rather than studying the propagation of the jet's head as it was done in the quoted papers. Our approach is thus also different from that of Jones et al. (1999) who solved a simplified version of the electron transport equation to account for shock diffusive acceleration and synchrotron aging in a time-dependent simulation of a radio lobe.

In studying the instability evolution, we adopt the so-called 'temporal' approach (see Bodo et al. 1994), in which one can

Send offprint requests to: M. Micono

follow the system evolution for longer times, as opposed to the 'spatial analysis' (see Hardee & Norman 1988a,b and Stone et al. 1997), in which one is limited by the transit time through the grid. While the spatial approach allows for more direct comparison with observations, the temporal analysis is preferred when studying the physics of the instability evolution over long time scales, with good spatial resolution and without exceedingly large computational domains.

The plan of the paper is the following: in the next section (Sect. 2), we describe the physical model for the jet, the main assumptions and the integration method; in Sect. 3 we deal with the treatment of the evolution equation for the relativistic electrons distribution and of the shock acceleration; the simulations results are discussed in Sects. 4 and 5 where a comparison between our model and observational data of extragalactic jets is presented, and the conclusions are given in Sect. 6.

2. The jet physical model

We consider a non-relativistic, fluid jet that propagates in a uniform medium and is in pressure equilibrium with its environment. This environment is permeated by a *passive* magnetic field, that is advected by the fluid and has no effect in the momentum conservation equation ($\beta_{\rm plasma} \to \infty$). Under these conditions, the relevant equations are the hydrodynamic equations of mass, momentum and energy conservation:

$$\frac{\partial \rho}{\partial t} + \nabla \cdot (\rho \boldsymbol{v}) = 0 \tag{1}$$

$$\frac{\partial \boldsymbol{v}}{\partial t} + (\boldsymbol{v} \cdot \nabla)\boldsymbol{v} = -\nabla p/\rho \tag{2}$$

$$\frac{\partial p}{\partial t} + (\boldsymbol{v} \cdot \nabla)p - \Gamma \frac{p}{\rho}\left[\frac{\partial \rho}{\partial t} + (\boldsymbol{v} \cdot \nabla)\rho\right] = 0 \ , \tag{3}$$

where, as usual, p represents the thermal pressure, ρ the density, $\mathbf{v}$ the fluid velocity, and Γ stands for the ratio of specific heats.

We then restrict our analysis to an infinite jet in cylindrical geometry (in the coordinates r, z); consistently with our assumptions, the equation system (1),(2),(3) can be complemented by the equations for the passive magnetic field, in the form:

$$\frac{\partial}{\partial t}(rA_\phi(r,z)) + \boldsymbol{v} \cdot \nabla(rA_\phi(r,z)) = 0 \tag{4}$$

$$\frac{\partial}{\partial t}\left(\frac{B_\phi(r,z)}{\rho r}\right) + \boldsymbol{v} \cdot \nabla\left(\frac{B_\phi(r,z)}{\rho r}\right) = 0 \, , \tag{5}$$

where $A_\phi(r,z)$ is the only component of the vector potential for B_z, B_r ($rA_\phi(r,z)$ is usually called 'stream function'), as appropriate for the chosen geometry, and $B_\phi(r,z)$ is the toroidal field. One can notice that Eqs. (4,5) have in common the standard form of a 'tracer' equation:

$$\frac{\partial \mathcal{T}}{\partial t} + \boldsymbol{v} \cdot \nabla \mathcal{T} = 0 \ , \tag{6}$$

where $\mathcal{T} \equiv rA_\phi$ in Eq. (4) and $\mathcal{T} \equiv B_\phi/\rho r$ in Eq. (5).

2.1. Initial configuration and boundary conditions

As mentioned before, we consider an axially symmetric, cylindrical jet. The flow velocity is initially uniform along the z direction (V_z) and the jet is in pressure equilibrium with the ambient medium. The initial velocity and density profiles in the r coordinate, and the perturbation to the transverse velocity $V_r(r,z)$ are the same as in Rossi et al. (1997).

In the calculations we measure lengths in units of the jet initial radius a, time in units of the radius sound crossing time $t_{\rm c} \equiv a/c_{\rm si}$ ($c_{\rm si}$ is the isothermal sound speed internal to the jet), and the magnetic field in units of the initial value B_0.

The initial configuration for the magnetic field is assumed poloidal (longitudinal) plus azimuthal:

$$B_z = 1 \, , \ B_r = 0 \, , \ B_\phi = \frac{2r}{\cosh(r^m)} \, , \tag{7}$$

with $m = 8$.

The system of Eqs. (1),(2),(3) is solved numerically by means of a PPM (Piecewise Parabolic Method) hydrocode (Colella & Woodward 1984) over an integration domain of 512×256 grid points, with the jet radius spanning over 60 grid points, for a total domain of $0 \le z \le 10\pi$, $0 \le r \le 20$. The axis of the jet is coincident with the bottom boundary of the domain ($r = 0$), where symmetric (for p, ρ, V_z and $B_\phi/(\rho r)$) or antisymmetric (for V_r and rA_ϕ) boundary conditions are given. At the $z = 0$ and $z = 20$ boundaries, consistently with the assumption of a infinite jet, we have set periodic conditions, and at the upper boundary ($r = R$) we have chosen a free outflow condition, by imposing for each variable null gradient ($d/dr = 0$). The grid in the r direction is non-uniform, but expands with r to avoid the effects of partial reflections at the top boundary (see Bodo et al. 1994 and Rossi et al. 1997).

3. Evolution of relativistic electrons

We study the evolution of a distribution of relativistic electrons as it is passively advected by the fluid. The relativistic electrons are assumed to be injected, at the initial time $t = 0$, with a power-law spectrum $N^*(E,0) = N_0^* E^{-\gamma}$, defined on an initial energy interval $10^{-4} < E/E_0 < 10^2$, where E_0 will be defined below. As the evolution proceeds, the electrons energy can vary on a wider interval $10^{-6} < E/E_0 < 10^4$. A would-be representative sample of $n = 10$ *parcels* of this distribution are then selected and followed, as *Lagrangian test particles*, as they travel with the fluid, undergoing adiabatic expansion/compression effects, synchrotron losses and shock acceleration.

3.1. Energy evolution equation

The temporal evolution equation for a distribution function $N^*(E,t)$ for the number of relativistic electrons present in a parcel, subject to adiabatic effects and synchrotron losses, can by written as (Kardashev 1962):

$$\frac{\partial N^*}{\partial t} = \frac{\partial}{\partial E}\left[\left(\alpha(t)E + \beta(t)E^2\right)N^*\right] \ , \tag{8}$$

where

$$\alpha(t) = \frac{1}{3}\,\nabla\cdot\boldsymbol{v}\,, \tag{9}$$

takes into account adiabatic effects, and

$$\beta(t) = bB^2\,, \tag{10}$$

accounts for synchrotron losses. Electron energy is expressed in units of the electron energy lost by synchrotron emission in a time unit in the initial magnetic field, $E_0 = 1/(bB_0^2 t_{\rm c})$.

Eq. (8) is solved numerically for the selected test parcels, away from shocks and at every time step, using a Lax-Wendroff scheme, and the coupling between Eq. (8) and the hydrodynamic equations (1) is given by the expansion/compression term $\nabla\cdot\boldsymbol{v}$, while the coefficient for synchrotron emission comes from the equations for the magnetic field evolution (4) and (5). The solution of the energy evolution equation is connected to the hydrodynamic evolution through a time-splitting technique, with an accurate control on the two Courant times.

We note that Kardashev (1962) gives an analytical solution for Eq. (8) under the hypothesis that the initial distribution function is a power-law. As time elapses, synchrotron losses and adiabatic effects modify the shape of the energy spectrum in the high and low energy ranges respectively, and therefore the spectrum evolves in time departing from a power-law. In absence of shocks, one could adopt the Kardashev solution at any time, but shocks introduce discontinuities in the evolution; when the parcel has crossed a shock wave, the new initial condition for the integration of Eq. (8) is the post-shock distribution function, which is not a power-law and thus does not fulfill the Kardashev (1962) prescriptions.

3.2. Diffusive shock acceleration

When the selected test particle, representing a parcel of the distribution, enters a shock, Fermi acceleration takes place. Under the assumptions that the acceleration time scale $t_{\rm acc}$ ($\sim \kappa/v^2$, with κ the spatial diffusion coefficient) is much smaller than both the synchrotron time $t_{\rm sync}$, and the dynamical time for shock evolution ($\sim t_{\rm c}$), we can apply the stationary diffusive shock acceleration (DSA) model (see for example Drury 1983 for a review). These conditions are fully verified in the energy interval over which our electron distribution is allowed to vary, as it was defined above.

The theory of diffusive shock acceleration relates the downstream particle spectrum $N_+(E,t)$ to the upstream particle spectrum $N_-(E,t)$ by (see for example Kirk 1994):

$$N_+(E,t) = q\,E^{-q+2}\int_{E_{\rm min}}^{E} N_-(E',t)\,E'^{\,q-3}\,dE'\,, \tag{11}$$

with

$$q = \frac{3r}{r-1}\,, \tag{12}$$

where $r = \rho_+/\rho_-$ is the shock compression ratio, and $E_{\rm min}$ is the minimum electron energy in the pre-shock spectrum.

Table 1. Initial positions of the particles in the domain.

particle	z	r
1	12.21	0.325
2	〃	0.5
3	〃	0.66
4	〃	0.825
5	〃	0.99
6	22.03	0.24
7	〃	0.41
8	〃	0.575
9	〃	0.74
10	〃	0.91

Table 2. Scaling parameters.

	Simulation
Magnetic field	$B_0 = 3\times10^{-5}$ Gauss
Jet radius	a = 100 pc
Sound velocity	$c_{\rm s} = 10^8$ cm s^{-1}
Particles scale energy	$E_0 = 0.21$ erg
Particles Lorentz factor	$\Gamma_0 = 2.55\times10^5$

In Eq. 8 and throughout we use the particle spectrum integrated over the volume $N^*(E,t)dE = N(E,t)V(t)dE$, following Kardashev (1962), and an additional factor $r = \rho_+/\rho_-$ needs to be included to take account of the change from number densities to numbers of particles. Thence we have:

$$N_+^*(E,t) = \frac{q}{r}\,E^{-q+2}\int_{E_{\rm min}}^{E} N_-^*(E',t)\,E'^{\,q-3}\,dE'\ . \tag{13}$$

We note that the post-shock energy spectrum is not a power-law any longer.

White (1985), Achterberg (1990), Schneider (1993) (see also the discussion in Melrose & Pope 1993) found that for an infinity of equally strong shocks with $r = 4$ and decompressions, the final distribution approaches $N_+^*(E) \propto E^{-1}$.

4. Results

We have carried out a simulation with a fluid jet defined by the following parameters: Mach number $\mathcal{M}(\equiv v_z/c_{\rm si}\sqrt{\Gamma}) = 5$, density ratio $\nu(\equiv \rho_\infty/\rho_{\rm jet}) = 5$. We studied the evolution of the energy spectra associated with 10 Lagrangian test particles, whose initial positions are given in Table 1; the initial spectral index for the distribution functions was $\gamma = 3.5$. Consistently with the assumed boundary conditions, particles leaving the domain on the right boundary at $z = 10\pi$ are re-injected at $z = 0$, and those leaving the domain at the upper boundary $r = 20$ are lost.

To extract some physical quantities from our results for a comparison with the observational data, we needed to fix the scale quantities, and these are summarized in Table 2. They have been selected within the ranges fixed by Birkinshaw (1991) for the parameters characterizing radio jets.

Table 3. Number of shocks crossed by a particle at a given time, and exponent of the electrons distribution function

particle	$t = 12$		$t = 16$		$16 < t < 22$	
	n	γ	n	γ	n	γ
1	5	2.3	10	1.6	13	3.6
2	3	2.7	8	1.8	10	3.4
3	1	3.2	6	1.8	9	2.1
4	1	7.	4	2.	7	4.4
5	0		3	5.	6	2.
6	4	2.2	7	1.8	10	1.6
7	3	2.6	5	1.9	8	2.4
8	3	3.2	6	2.	11	1.6
9	1	6.2	2	2.4	7	1.8
10	1	7.	2	2.	5	1.9
r	1.5–2.5		~ 4		2.5–1.5	

4.1. Instability evolution

As described in detail in Bodo et al. (1994) the perturbed jet undergoes three stages of the instability:

Linear phase ($\mathrm{time} \leq 7$): the unstable modes excited by the perturbation grow in accord with the linear theory. In the latter portion of this stage the growth of the modes leads to the formation of internal shocks.

Acoustic phase ($7 < \mathrm{time} \leq 17$): the growth of internal shocks is accompanied by a global deformation of the jet; energy and momentum are transferred from the jet to the external medium through acoustic waves.

Mixing phase ($\mathrm{time} > 17$): as a consequence of the shock evolution, mixing between jet and external material begins to occur.

If the simulation is carried out further, a final statistically quasi-stationary stage is attained.

4.2. Particle spectrum evolution

We now analyze the behavior of the Lagrangian particles and the evolution of the energy spectra of the relativistic electrons as these particles are advected through the different stages of the instability evolution. We selected three typical times, $t = 12$ in the middle of the acoustic phase, $t = 16$ at the end, and $t = 22$ when the mixing is already developed; the number of shocks crossed by each particle at these given times, the average compression ratios of these shocks and the power index of the distribution functions are given in Table 3. The details of the shock number and strength for each particle in each phase can be inferred from Fig. 1.

In Fig. 2 we show three images of the jet density, in a logarithmic grey-scale, at these selected times, with superimposed the positions of the Lagrangian particles, identified by different symbols. The vectors give the module and directions of the particles' velocities. In Fig. 3 we plot the distribution functions associated to some of the Lagrangian particles at the initial time and after the acceleration and loss processes, at the same times selected above.

During the linear phase the particles advance advected by the fluid and the relativistic electrons lose energy through adiabatic expansion and synchrotron radiation. The energy spectra steepen and the maximum energy diminishes, as can be seen, for example, from the spectrum associated to particle 5 at time $t = 12$ (continuous line in Fig. 3), when this particle has not crossed any shock yet.

When shocks start to form, electrons are accelerated. The first acceleration process occurs for the distribution function associated to particle 1 at time $t = 8.33$. At time $t = 12$ only the particles initially located at a distance less than 0.7 jet radii from the jet axis have crossed a significant (~ 4) number of shocks; at this stage shocks are still weak, with compression ratios not exceeding $r \sim 2.5$, and the electrons are only weakly accelerated; from Table 3 we see that the energy spectrum is a power law slightly flatter than the initial one. The particles located on the jet edges initially, instead, cross one or two shocks at most, and their spectrum is still very steep ($\gamma \sim 6$) due to the losses that occurred in the linear phase of the evolution.

At time $t = 16$ the jet is at the end of the acoustic phase; the Lagrangian particles have crossed a high number of shocks (on average ~ 6, up to 10 for particle 1). Many of these shocks are very strong, with compression ratios $r \sim 4$, and the acceleration process is very efficient as can be inferred from the values of the spectral index, which lies at this stage in the interval $1.5 \lesssim \gamma \lesssim 2$.

There are three main reasons why particles whose initial position is located near to the jet axis undergo a higher number of shock accelerations: first, their longitudinal velocity is higher with respect to the particles located on the edges of the jet; second, their trajectory is less affected by motions in the radial direction, since, due to the assumed geometry, the value of the radial velocity approaches zero near to the jet axis (see also Fig. 2); third, the shocks that form due to the non linear growth of the symmetrical body modes of the Kelvin-Helmholtz instability are biconical shocks whose vertex is located on the jet axis, and so the distance between shocks is smaller near the axis than near the edges.

After time $t = 16$ the jet material starts to mix with the external medium, shocks become less frequent and weaker (compression ratios $r \sim 2$), until time $t = 22$ when the mixing is well developed; shocks are encountered less frequently by the particles, whose velocity is diminished with respect to the initial velocity, see Fig. 2c. The spectral index of the electrons distribution functions is different for the various particles: those which cross a small number of shocks acquire a steep spectral index, comparable to the initial one (ex. particles 1,2,4,7) while those which cross a conspicuous number of shocks show a flatter spectrum ($\gamma \sim 2$; compare the values in the last column of Table 3 and Fig. 1).

As the evolution progresses further, the mixing process between the jet and the external medium dominates; the jet velocity decreases, while momentum is transferred to the external medium, and shocks lose strength until they disappear (see Fig. 2c). The motion of the particles is no longer ordered, they can be trapped in vortices and cross regions of high magnetic field where electrons lose energy via synchrotron radiation with

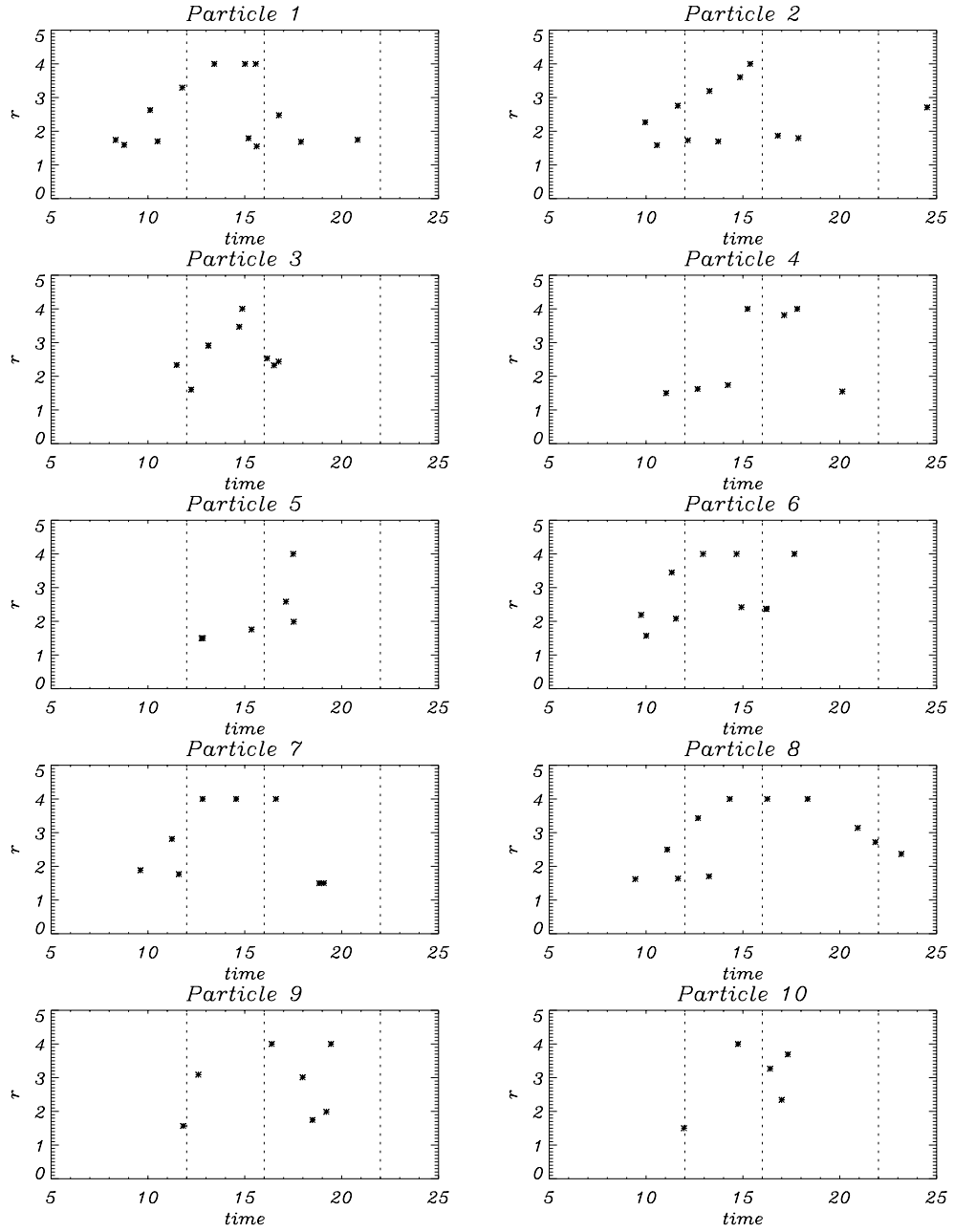

Fig. 1. Compression ratio of each shock crossed by the Lagrangian particles as a function of time. The dashed lines are traced at the three typical times $t = 12$, $t = 6$ and $t = 22$ selected for the analysis and representative of different stages in the evolution. From this figure the number and strength of the shocks can be inferred.

no acceleration mechanism at work. In Fig. 4 we show the trajectory of the Lagrangian particles as a function of the distance from the point of injection; observe the 'loops' that appear in their paths, and how they move far away from the jet axis, as the jet itself expands and entrains external medium. The 'dots' on the paths in Fig. 4 are snapshots of the particles' position at fixed time intervals (corresponding to one time-scale): see how their velocity diminishes as they move further downstream along the jet. As we extend our study further in time, the electron spectrum steepen and the spectrum moves towards lower and lower energies, approaching the non-relativistic limit.

An important consequence of our model is the conservation of the total number of relativistic electrons. We calculated the integral of the electron distribution functions and found that it does not vary of more than the 2% of the initial value during the different stages of the evolution. This implies that no further injection of relativistic particles after the initial one at the jet's source is needed; a finite, relatively small, number of shocks is able to reaccelerate the electrons even if their maximum energy is lowered and their energy spectrum is steepened by synchrotron and expansion losses.

5. On observable quantities

From the results described in the previous section, we can deduce some important values and trends that can be directly compared to some observable quantities characterizing extragalactic radio sources. We compare the values obtained from our calcu-

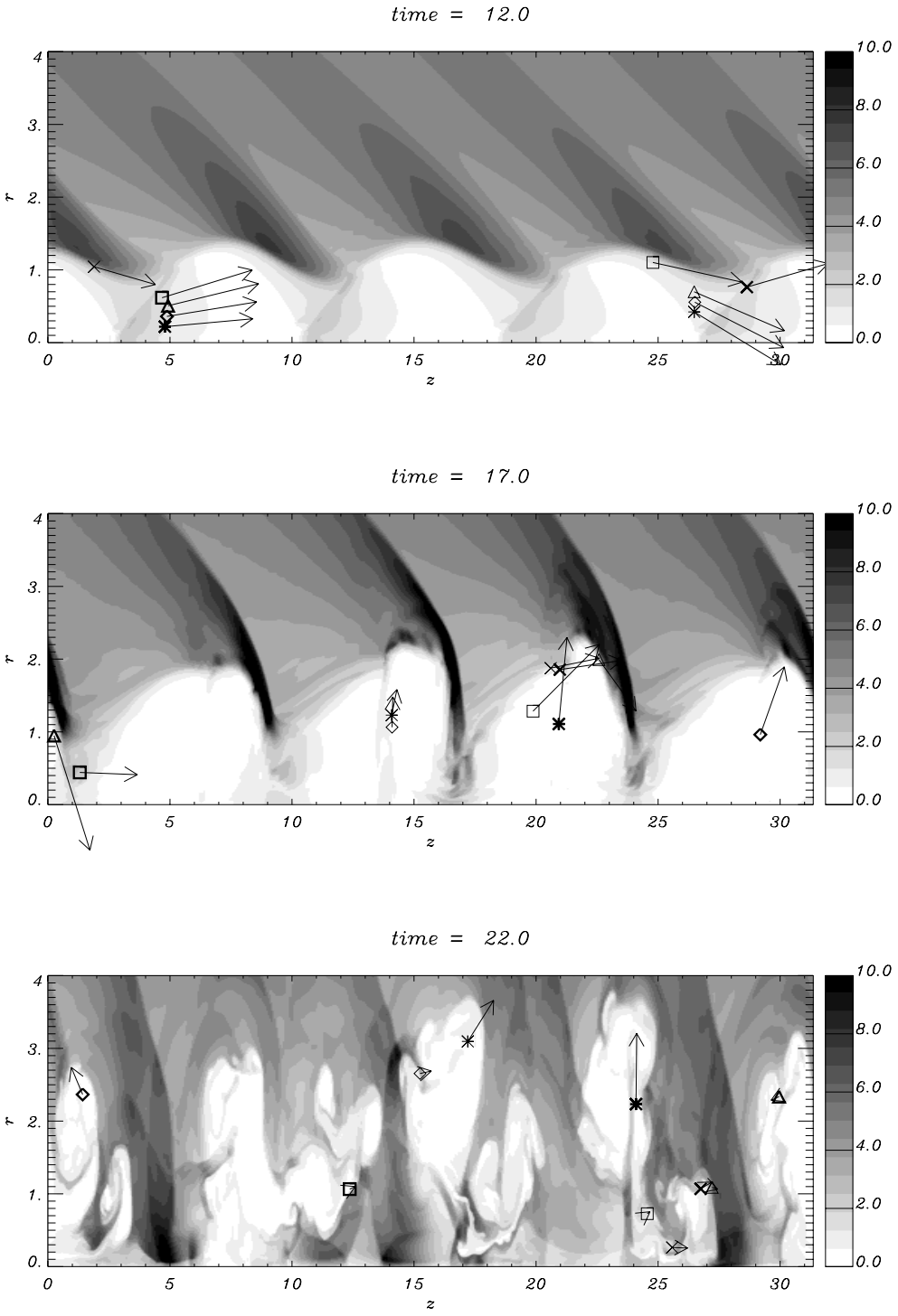

Fig. 2. Grey-scale images of the jet density at three selected times. The jet axis is located on the lower horizontal boundary of the domain. The symbols superposed to the images show the positions of the 10 Lagrangian particles, and the vectors represent their velocity.

lations to those available for some well studied radio jets. It is important to notice that some of these sources have been recognized to be relativistic (e.g. 3C 273, jet Lorentz factor $\Gamma_{\rm jet} \gtrsim 10$, Zensus et al. 1990) or weakly relativistic (e.g. M 87, $\Gamma_{\rm jet} \lesssim 2.5$, Reid et al. 1989, Biretta et al., 1995), while our calculations are performed under the hypothesis that the bulk jet material is a non-relativistic thermal gas. We expect that relativistic velocities introduce some important dynamical differences, regarding mainly the growth rates of the instability (Ferrari et al. 1978), and the properties of shock waves that form (Bicknell & Begelman 1996). Moreover, the standard diffusion approximation that we adopted to study the particle acceleration at shocks does not stand when shocks are relativistic: the anisotropy of the particle distribution function must be taken into account and the general solution of the transport equation must be constructed (Kirk & Schneider 1987). In the relativistic case the resulting spectrum of the accelerated particles has a strong dependence on the shock compression ratio, and a small, though significant dependence

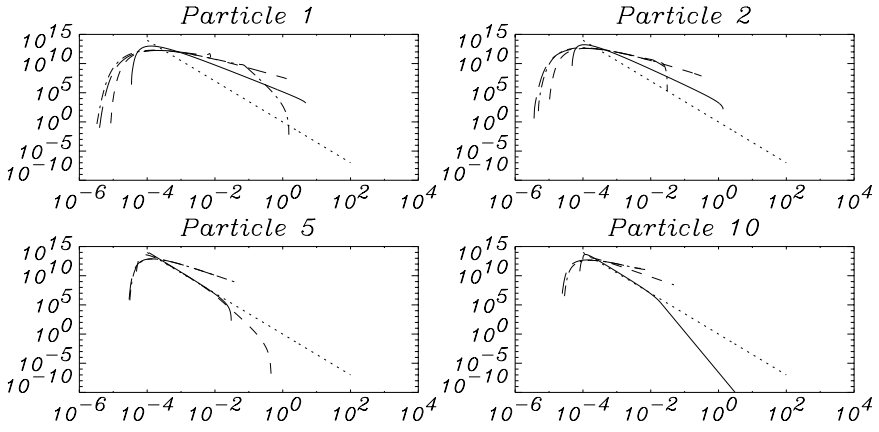

Fig. 3. Energy spectra of the electrons associated to the Lagrangian particles 1,2,5 and 10, at three selected times. The dotted line represents the initial spectrum, the solid line is for $t = 12$, the dashed line for $t = 16$ and the dash-dotted line is for $t = 22$.

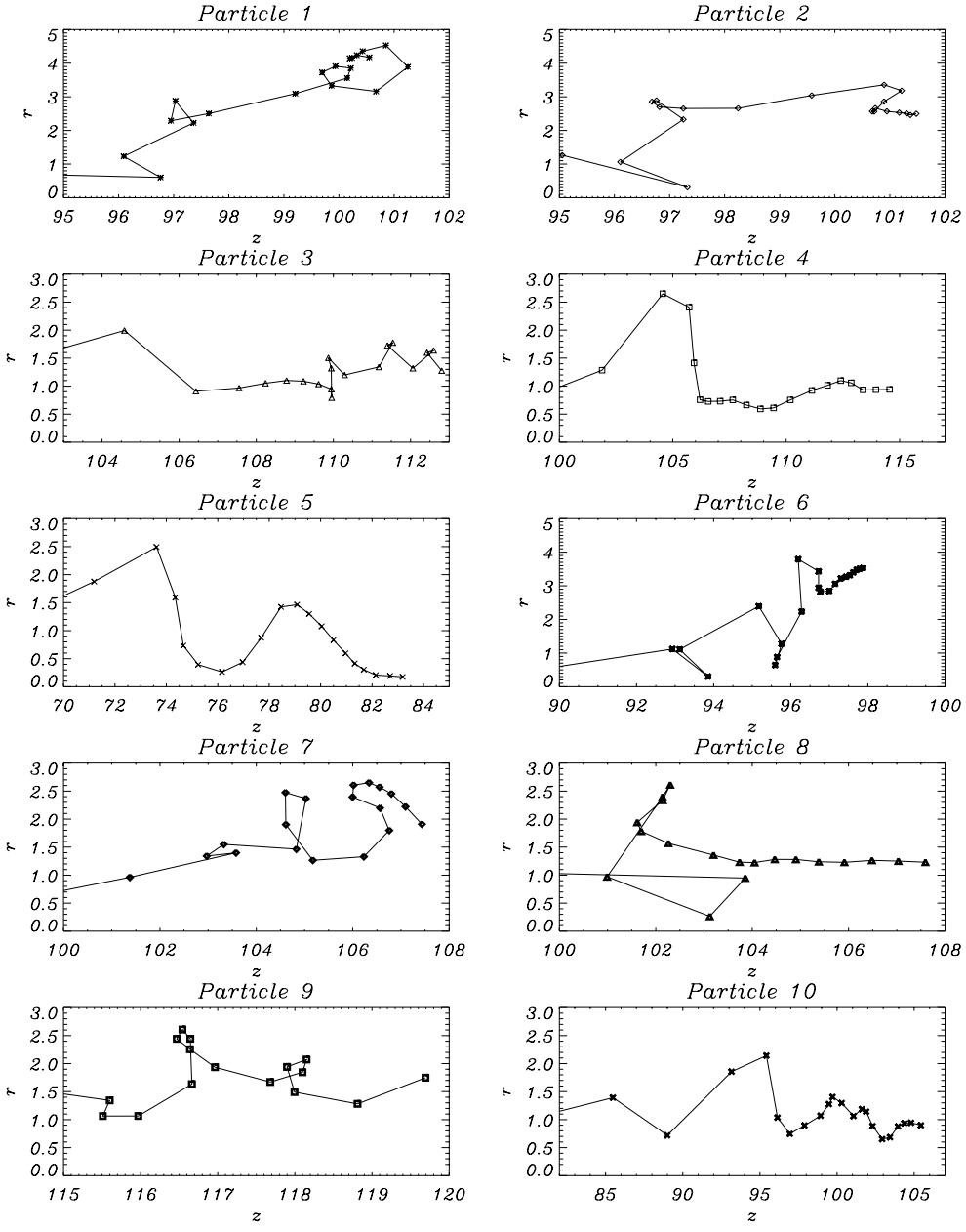

Fig. 4. Trajectories of the ten particles plotted as a function of distances from the injection point. Only the final sections of the trajectories are represented, since in previous stages the particles travel along a direction almost parallel to the jet axis, at a distance equal to the initial transversal position.

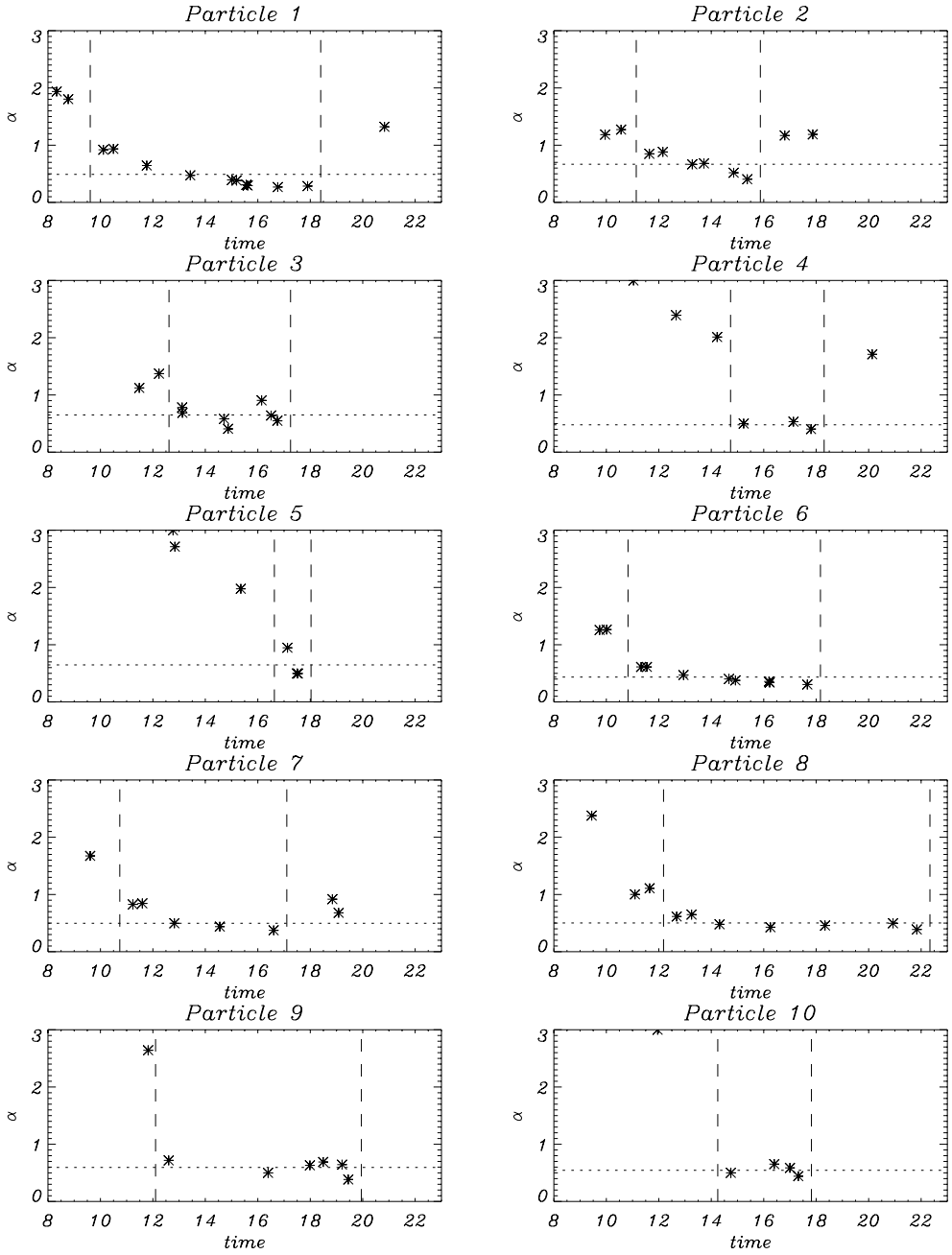

Fig. 5. Post-shock radio (frequency interval: $10^9 \lesssim \nu \lesssim 6. \times 10^{11}$ Hz) spectral index, at each shock crossed by each Lagrangian particle. The dotted lines correspond to the values obtained by averaging over the shocks crossed in the time intervals defined by the dashed lines, and reported in the second column of Table 4.

on the form of the assumed diffusion coefficient (Heavens & Drury 1988). However if shocks that form are oblique, as in the case of the Kelvin-Helmholtz induced biconical shocks, the *shock velocity* is reduced, with respect to the jet velocity, by a geometrical factor; in this way the *shock* Lorentz factor can be significantly smaller than the *jet* Lorentz factor; Heavens & Drury (1988) find that the non-relativistic treatment for particle acceleration at shocks gives a reasonable estimate for the spectral index for shock Lorentz factors up to ~ 1.15: our results are thus valid also for weakly relativistic jets, provided that shocks in the flow are oblique, as it seems to be the case of knot A in M87 (Bicknell & Begelman 1996).

Our results allow us to calculate the spectral index of the radiation emitted by the synchrotron mechanism, in different frequency intervals. In Table 4 we show the values of the radiation spectral index for the 10 particles in those frequency ranges that are relevant for observations, i.e. radio, radio-optical and optical-UV. The values in Table 4 are average values of the spectral index calculated by fitting the post-shock electrons spectra with a power law, and averaging the values in a temporal interval corresponding to the shock-dominated phase of the jet's evolution.

At radio frequencies, we find that the spectral index varies in the range $0.43 \lesssim \alpha_r \lesssim 0.67$, consistently with the values found

Table 4. Average spectral indexes for the 10 parcels in radio, radio to optical and optical-UV frequency ranges

particle	radio	radio-opt	opt-UV
1	0.49	0.71	0.96
2	0.67	0.89	1.13
3	0.65	0.74	0.83
4	0.48	0.49	0.51
5	0.65	0.65	0.65
6	0.43	0.55	0.76
7	0.50	0.58	0.71
8	0.50	0.70	0.83
9	0.59	0.82	1.00
10	0.54	0.61	0.71

in the majority of radio jets (see for example Bridle & Perley 1984).

Only a few sources can be detected at optical frequencies, and thus the data on radio to optical spectral index are available only for M87 ($0.61 \leq \alpha_{ro} \leq 0.76$, Sparks et al. 1996), 3C273 ($\alpha_{ro} \sim 0.82$, Meisenheimer at al. 1996), 3C31 ($\alpha_{ro} \sim 0.8$, Fraix-Burnet et al. 1991a), 3C66B ($0.60 \leq \alpha_{ro} \leq 0.75$, Fraix-Burnet et al. 1991b), and for other three cases (3C 147, 3C 239 and 3C 433) which show a radio to optical spectral index significantly higher. From Table 4, the average spectral indexes associated to our particles in the radio to optical frequency range ($10^9 \leq \nu \leq 7.7 \times 10^{14}$ Hz) are consistent with the first class of objects, and are in the interval: $0.55 \lesssim \alpha_{ro} \lesssim 0.89$.

Finally, recent HST observations of the M87 jet by Sparks et al. (1996) allowed the authors to estimate the value of the spectral index in the optical-UV band, in the range of frequencies observed by the FOC detector on board HST ($5.6 \times 10^{14} \leq \nu \leq 2 \times 10^{15}$ Hz), $\alpha_{o-UV} \sim 1.3$. In these frequency intervals our values span from $\alpha_{opt,o-UV} \sim 0.51$ to ~ 1.13.

In Fig. 5 we show the values of the radio spectral index calculated at each shock for each of the 10 Lagrangian particles. The dotted lines define the time intervals used in Table 4. From the figure it is clear how the spectral index starts from an initially high value (here the first linear phase is not represented, and so the values derived from the values of γ at $t = 12$ in Table 3 are not shown), and it decreases as the particles enter a higher and higher number of shocks, during the acoustic phase of the instability.

When the jet enters the mixing phase, shocks become rare and weak, and the spectral index increases. This is an interesting point, because the final increase in the spectral index is a feature which comes out from the evolution of the instability, and does not depend on the initial parameters or assumptions of our model; on the contrary, assuming a different initial slope for the electrons spectrum could give a different trend for the spectral index in the shock-dominated region of the jet: for example, if the electrons were injected directly at the beginning of the acoustic phase, they would not undergo the heavy losses and steepening as happens in the first linear phase of the evolution; a different trend could also be obtained abandoning the assumption of Lagrangian advection of the particles by the fluid, or if, following a different choice of the initial jet parameters, many more shocks were involved or shocks with stronger compression ratios. In this way, the decreasing trend would be probably limited to the first section of the knots chain, and would be followed by a region of quasi-constant or increasing spectral index.

This behavior is in agreement with the trend in the radio spectral index observed in a number of extragalactic radio jets: for example, Sparks et al. (1996) and Meisenheimer et al. (1996) show that in M87 the spectral index oscillates around the mean value for the first section of the knot chain, and increases for the farthest knots from the source, and this is a feature common to all the frequency ranges that were studied; in NGC 6251 the spectral index is almost constant along the jet, with oscillations around the mean value $\alpha \sim 0.6$, and it shows a gradual steepening to 0.8 shortly before the jet widens up and mixes with the diffuse lobe emission (Mack et al. 1998) and Perley et al. (1984); similar values and trends are also observed in Cen A (Burns et al. 1983), 3C 279 (De Pater & Perley 1983) and 3C 31 (Strom et al. 1983).

Fig. 5 and Table 3 show that the value reached by the spectral index is not strictly correlated to the initial radial position of the Lagrangian particle in the jet: a small number of close strong shocks can flatten the electron energy spectrum in the same way as a higher number of distributed shocks. The particles initially located nearer to the jet axis, nevertheless, show a quasi-constant spectral index for a longer time: compare for example particles 1,2,6,7,8 which cross a high number of shocks, to particles 4,5,9,10 whose spectrum is flat instead only for a limited interval of time.

In Fig. 6 the values and evolution of the spectral index α associated to particle 1 in the different frequency ranges are compared. Energetic electrons undergo synchrotron losses more rapidly, and the high energy section of the spectrum steepen more quickly. This leads to a higher average value of the spectral index in the optical-UV region respect to the radio value and a shorter temporal (and thus spatial) extent of the region where the spectrum is flatter; α_{o-UV} starts to grow already before the onset of the mixing phase.

Fig. 7a shows the behavior of the spectral index α for the post-shock distribution function (stars) as well as for the inter-knot regions (continuous line). In Fig. 7a the temporal evolution has been translated into a spatial evolution, and the values of the spectral index are plotted as a function of the distance of the particle from the injection point. The trend in Fig. 7a reproduces qualitatively the behavior of the optical and radio-optical spectral index observed by Meisenheimer et al. (1996) for M87, although in our model the oscillations between the values in knot and inter-knot regions have a bigger amplitude at the beginning of the shock chain, while just before the onset of the mixing phase the pattern is almost constant; in M87, which is the only object which can be observed with enough resolution to provide these data, the knot to inter-knot differences are always smaller than $\Delta\alpha \sim 0.2$, while in our case the average value is $\Delta\alpha \sim 0.23$.

Fig. 7 only shows the section of the jet where shocks are present. The first section, where the perturbation grows according to the linear theory, corresponds to the *gap* between the

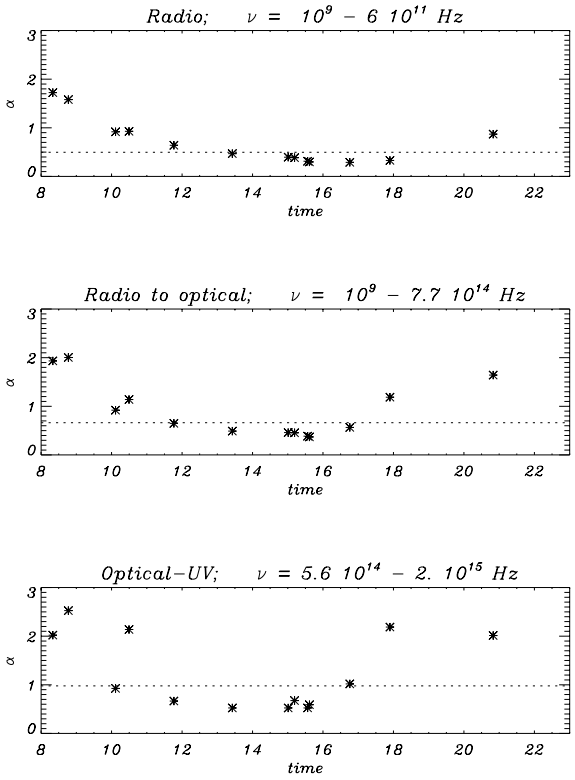

Fig. 6. Radio, radio to optical and optical to UV post-shock spectral indexes calculated for particle 1. The dotted lines show, as in Fig. 5, the average values calculated in the time interval $9.5 \lesssim t \lesssim 18.5$, corresponding to the shock-dominated stage of the evolution

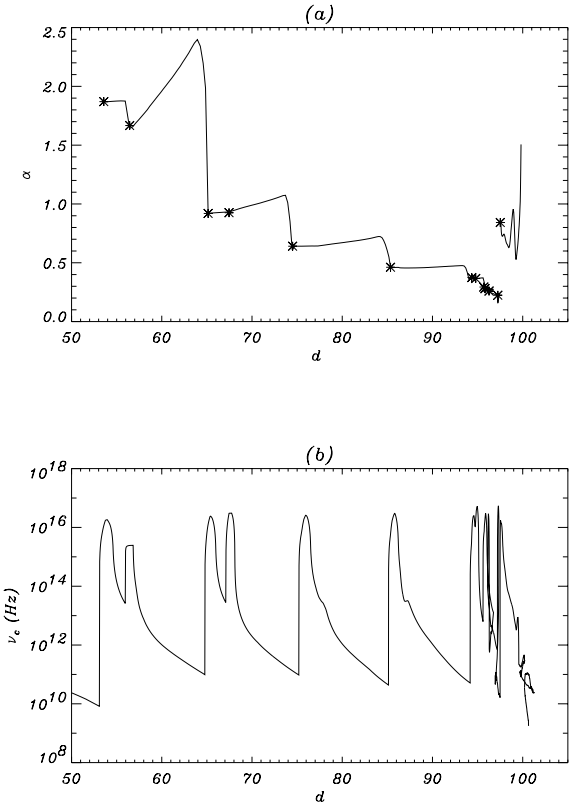

Fig. 7. Panel **a**: variation in the spectral index values with distance from the jet injection point, for the electron distribution function associated with particle 1. The stars represent the post-shock values of the spectral index. Panel **b**: Cutoff frequency in the electron distribution function as a function of the distance from the jet injection point.

source and the first bright knot observed in most astrophysical jets. If we adopt for the jet radius an average value estimated for a typical radio jet (see Table 2) we find consistent values for the inter-shock distances between our model and the inter-knot distances that are generally observed, while the length of the emission gap in our model is an order of magnitude larger than observed. However, we recall that the simple cylindrical geometry adopted here forces us to select an average, constant value for the jet radius (and for all the physical parameters in general), while it is well known that in the inner regions the jet radius can be up to two orders of magnitude smaller (in the case of M87, for example, the jet radius is below the HST 0.03″ resolution (i.e. $\lesssim 2.5$ pc) close to the source, Biretta (1998), and increases with distance with an opening angle 5–7° at VLA wavelengths). Bearing this in mind, a gap of ~ 50 jet radii from the source, where the first shock forms, would correspond to a distance consistent with the gaps that are currently observed in radio jets.

Finally, Fig. 7b shows the spatial trend of the cutoff frequency $\nu_c = 4.3 \times 10^6\ B_\perp \Gamma^2$ Hz as it results from the evolution of the cutoff energy along the jet for particle 1. The values of the peaks in Fig. 7b are model-dependent, i.e. they depend on the maximum value that the electron energy can attain in our model since we assume that at shocks the electrons are re-accelerated up to the initial maximum energy value $\Gamma_{\max} = 100\ \Gamma_0 \sim 2.55 \times 10^7$. This assumption only influences the peak values: other simulations performed assuming different values for the maximum allowed energy gave a similar trend, with different peak heights (but the same widths).

Our results imply that while the knots regions are bright at least up to optical frequencies, in the inter-knot regions only radio emission can take place. Therefore, as long as the cutoff frequency is concerned, our simplified model does not explain the features observed in the M87 jet, where Meisenheimer et al. (1996) find that the cutoff frequency in the inter-knot regions lies in the optical region of the spectrum. The authors report that the cutoff frequency changes by no more than a factor 3 along the jet. Even if we smooth our data at the resolution of Meisenheimer et al. we still find variations in ν_c of two orders of magnitude, and $\nu_c \leq 10^{12}$ in the inter-knot regions, rendering them optically invisible.

6. Conclusions

We presented a self-consistent study of particles shock acceleration, in the test particle approximation, in an astrophysical jet.

We found that the non linear growth of the Kelvin-Helmholtz instability is able to produce a high number (~ 10) of strong shocks where the energy of a distribution of relativistic elec-

trons advected by the fluid can be increased via the first order Fermi-like mechanism of diffusive shock acceleration. The acceleration process is efficient enough to compete with the losses via synchrotron radiation and adiabatic expansion taking place in the whole body of the jet; the flattening in the energy spectrum of the electrons gives rise to a flat frequency spectrum of the synchrotron radiation emitted which can be directly compared with observations.

We discussed the acceleration process connected to the subsequent phases of the instability evolution; involving 10 Lagrangian parcels of the same initial distribution function located at different initial positions allowed us to find that the acceleration process is not dependent on the initial distance of the particles from the jet axis. Moreover we found that the total number of relativistic electrons associated with each Lagrangian particle is conserved during the whole evolution, up to the final stages when shocks cannot form any more and the electrons simply lose energy becoming non-relativistic.

A further improvement of our model would be the adoption of a numerical code written to solve the full magnetohydrodynamical equations: this would give the proper evolution of the magnetic field, whose components in our calculations are simply advected by the fluid. A situation in which the force exerted by the magnetic field on the fluid is taken into account could probably lead to a reduction of the shock strength, but it might also imply a longer duration of the shock-dominated phase of the instability evolution. The problems arising in the development of a reliable multidimensional MHD code have up to now limited the numerical study of magnetized jets.

From our results we were able to evaluate the average values for the spectral index of the emitted synchrotron radiation in different frequency ranges, obtaining values consistent with those derived from observations of extragalactic jets. We also gave estimates of the cutoff frequency expected in the knots and in the inter-knot regions of the jet.

Although the main aim of this work was to give a physical description of how the diffusive acceleration mechanism can work in a Kelvin-Helmholtz unstable jet, we could also derive the trends of the above described observational quantities with the position along the jet axis, and this was achieved translating our results in time into behavior with space. It is necessary to keep it into account when we refer for example to Fig. 7: the plots in Figs. 7a and 7b are not snapshots of the jet at a certain time, but are obtained following a parcel of the jet material as it moves downstream, thus evolving both in space and in time. For a more realistic application to observational data of the mechanism described in this paper, a 'spatial' analysis of the evolution of a jet propagating in a medium with decreasing density is required, in order to obtain snapshots of the whole (non-cylindrical) jet at selected times; this implies the adoption of large grids (see for example Micono et al., 1998) and consequently of a large number of Lagrangian particles, to cover with a good statistic the whole jet body; in this way we could also obtain indications on the variation of the density of the Lagrangian particles in different jet zones, and thus on their relative brightness. This study will be the subject of a future work.

References

Achterberg A., 1990, Physical Processes in Hot Cosmic Plasmas. Kluwer Academic Publishers, 67

Bell A.L., 1978, MNRAS 182, 147

Bicknell G.V., Begelman M.C., 1996, ApJ 467, 597

Biretta J.A., 1998, Private communication

Biretta J.A., Zhou F., Owen F.N., 1995, ApJ 447, 582

Birkinshaw M., 1991, In: Hughes P.A. (ed.) Beams and Jets in Astrophysics. Cambridge University Press, 278

Bisnovatyi-Kogan G.S., Lovelace R.V.E., 1995, A&A 296, L19

Blandford R.D., Eichler D., 1987, Physics Reports 154, 1

Bodo G., Massaglia S., Ferrari A., Trussoni E., 1994, A&A 283, 655

Bridle A.H., Perley R.A., 1984, ARA&A 22, 319

Burns J.O., Feigelson E.D., Schreier E.J., 1983, ApJ 273, 128

Colella P., Woodward P.R., 1984, J. Comp. Phys. 54, 174

De Pater I., Perley R.A., 1983, ApJ 273, 64

Drury L. O'C., 1983, Rep. prog. Phys. 46, 973

Ferrari A., Trussoni E., Zaninetti L., 1978, A&A 64, 43

Ferrari A., Melrose D.B. 1997, Mem. Soc. Astron. Ital. 68, 171

Fraix-Burnet D., Golombeck D., Macchetto F.D., et al., 1991a, AJ 101, 88

Fraix-Burnet D., Golombeck D., Macchetto F.D., 1991, AJ 102, 562

Hardee P.E., Norman M.L., 1988a, ApJ 334, 70

Hardee P.E., Norman M.L., 1988b, ApJ 334, 80

Heavens A.F., Drury L.O'C., 1988, MNRAS 235, 997

Jones T.W., Ryu D., Engel A., 1999, ApJ 512, 105

Kardashev N.S., 1962, SvA 6, 317

Kirk J.G., Schneider P., 1987, ApJ 315, 425

Kirk, J.G., 1994, Plasma Astrophysics. Saas-Fee Advanced Course 24 (Lecture Notes 1994), Springer-Verlag, Berlin, 225

Lesch H., Birk G.T., 1998, ApJ 499, 167

Li H., Miller J.A., Colgate S.A., 1997, Relativistic Jets in AGNs, Proceedings of the International Conference, 162

Mack K.H., Klein U., O'Dea C.P., Willis A.G., Saripalli L., 1998, A&A 329, 442

Massaglia S., Bodo G., Ferrari A., Rossi P., 1996, Jets from Stars and Galactic Nuclei. Proceedings of a Workshop Held at Bad Honnef (3–7 July 1995), 275

Matthews A.P., Scheuer P.A.G., 1990a, MNRAS 242, 616

Matthews A.P., Scheuer P.A.G., 1990b, MNRAS 242, 623

Meisenheimer K., Röser, H.-J., Schlötelburg M., 1996, Jets from Stars and Galactic Nuclei. Proceedings of a Workshop Held at Bad Honnef (3–7 July 1995), 231

Meisenheimer K., Neumann M., Röser H.-J., 1996, A&A 307, 61

Melrose D.B., Pope M.H., 1993, Proc. Astron. Soc. Australia 10, 222

Micono M., Massaglia S., Bodo G., Rossi P., Ferrari A., 1998, A&A 333, 989

Ostrowsky M., 1990, A&A 238, 435

Ostrowsky M., 1998, A&A 335, 134

Perley R.A., Bridle A.H., Willis A.G., 1984, ApJS 54, 291

Reid M.J., Biretta J.A., Junor W., Muxlow T.W.B., Spencer R.E., 1989, ApJ 336, 112

Rossi P., Bodo G., Massaglia S., Ferrari A., 1997, A&A 321, 672

Schneider P., 1993, A&A 278, 315

Sparks W.B., Biretta J.A., Macchetto F., 1996, ApJ 473, 254

Stone J.M., Xu J., Hardee P.E., 1997, ApJ 483, 136

Strom R.G., Fanti R., Parma P., Ekers R.D., 1983, A&A 122, 305

White R.L., 1985, ApJ 289, 698

Zensus J.A., Unwin S.C., Cohen M.H., Biretta J.A., 1990, AJ 100, 1777